



Temperature dependant polycrystal model application to bainitic steel behavior under tri-axial loading in the ductile–brittle transition

Maximilien Libert^{a,b}, Colette Rey^{a,*}, Ludovic Vincent^b, Bernard Marini^b

^a Laboratoire de Mécanique des Sols, Structures et Matériaux, CNRS, UMR 8579, École Centrale Paris, 92295 Châtenay-Malabry, France

^b Commissariat à l'Énergie Atomique, DEN/SRMA, 91191 Gif-sur-Yvette, France

ARTICLE INFO

Article history:

Received 24 November 2010

Received in revised form 16 February 2011

Available online 1 April 2011

Keywords:

Polycrystal plasticity

Steel

Mechanical behavior

Bainite

Cleavage fracture

Fracture probability

Pressure vessel steel

Constraint effect

ABSTRACT

A polycrystal finite element (FE) model describing the temperature evolution of low carbon steel is proposed in order to forecast the local mechanical fields as a function of temperature, for bainitic microstructure submitted to tri-axial loading. The model is designed for finite strains, large lattice rotations and temperatures ranging into the brittle–ductile transition domain. The dislocation densities are the internal variables. At low temperature in Body Centred Cubic (BCC) materials, plasticity is governed by double kink nucleation of screw dislocations, whereas at high temperature, plasticity depends on interactions between mobile dislocations and the forest dislocations. In this paper, the constitutive law and the evolution of the dislocation densities are written as a function of temperature and describe low and high temperature mechanisms. The studied aggregates are built from Electron Back Scattering Diffraction (EBSD) images of real bainitic steel. The aggregate is submitted to a tri-axial loading in order to describe the material at a crack tip. Mechanical parameters are deduced from mechanical tests. The local strain and stress fields, computed for different applied loadings, present local variations which depend on temperature and on tri-axial ratio. The distribution curves of the maximal principal stresses show that heterogeneities respectively increase with temperature and decrease with tri-axial ratio. A direct application of this model provides the evaluation of the rupture probability within the aggregate, which is treated as the elementary volume in the weak link theory. A comparison with the Beremin criterion calibrated on experimental data, shows that the computed fracture probability dispersion induced by the stress heterogeneities is of the same order than the measured dispersion. Temperature and stress tri-axiality ratio effects are also investigated. It is shown that these two parameters have a strong effect on fracture owing to their influence on the heterogeneous plastic strain. These inhomogeneities can initiate cleavage fracture.

© 2011 Elsevier Ltd. All rights reserved.

1. Introduction

Several crystal plasticity models were already developed to describe the effects of microstructure on mechanical fields and orientation textures (Peirce et al., 1983; Beaudoin et al., 1995; Tabourot et al., 1997; Barbe et al., 2001a,b; Hoc et al., 2001; Bhattacharyya et al., 2001; Stainier et al., 2002; Eriau and Rey, 2004). These polycrystal plasticity approaches did not explicitly describe the temperature effect on plasticity.

The main contribution of this paper is to include the mechanisms of plasticity depending on temperature in a BCC polycrystal model. The aim of our approach is to describe the local stress strain field evolution of a complex microstructures such as bainite with

temperature and loading. At low temperature, plastic deformation is controlled by the mobility of screw dislocations, whereas at high temperature, plastic deformation hardening results from interactions between the mobile dislocations and the forest dislocations (Kocks et al., 1975; Kubin et al., 1978). The transition temperature separating these two mechanisms of deformation belongs to the brittle–ductile transition of low carbon steel. For a given microstructure, the model can predict the domains undergoing larger principal local stresses (thus, more sensitive to damage).

The model is designed within the framework of finite plastic strain and of large lattice rotation. It is based on a viscoplastic constitutive law for each slip system and depends on internal variables: the dislocation densities. The model is implemented in Abaqus® FE code.

The evolution of local behavior depends on:

- Thermally activated flow laws, based on two different mechanisms, according to the involved temperature. At low temperature, a double kink mechanism (due to the lattice friction

* Corresponding author. Address: Laboratoire de Mécanique des Sols, Structures et Matériaux, CNRS, UMR 8579, École Centrale Paris, grande rue des vignes, 92295 Châtenay-Malabry, France. Tel.: +33 1 41 13 15 73.

E-mail address: colette.rey@ecp.fr (C. Rey).

effect), rules the motion of screw dislocations (Louchet, 1976; Rauch, 1993). At high temperature, the interactions between moving dislocations and forest obstacles rule the hardening mechanism.

- Dislocation densities evolution law. This evolution law is composed of two terms corresponding to the production and the annihilation of dislocations (Estrin and Mecking, 1984).

The model is applied to a low alloyed steel (A508C13) presenting a bainitic microstructure. The alloy composition is given in Section 3.1. The representative aggregates were built by Electron Back Scattering Diffraction (EBSD) mappings. They were submitted, to different tri-axial loadings corresponding to the loading state at the head of a Compact Tension sample micro-crack. The temperature ranges from -196°C to 25°C .

Determination of the model parameters is based on appropriate mechanical tests through an inverse method. The crystalline orientations and lath morphologies are obtained by EBSD technique and dislocation densities are measured by TEM.

The main purpose of this model is to obtain histograms and maps of the heterogeneous local strain and stress fields. An output of our results is a better understanding of cleavage mechanisms for bainitic low alloy steels (frequently used in nuclear pressure vessels). The complexity of the microstructure of such alloys leads to fracture toughness scattering. Thus, such studies at the grain level are crucial to assess the vessel integrity. Different authors (Brozzo et al., 1978; Curry and Knott, 1978; Beremin, 1983; Zhang and Knott, 1999) observed a scattering of fracture stresses mainly resulting of particle size distribution. More recently, other authors (Yang et al., 2004; Tanguy et al., 2003, 2005; Lee et al., 2002; Hausild et al., 2005) showed that the initiation of brittle fracture involves multiple microstructural crack initiators, such as lath packets boundaries, carbides or manganese sulfides. All these papers suggested that the metallurgical features involved in the cleavage initiation might change from the lower shelf up to the ductile/brittle transition regime. Moreover, Hausild et al. (2005), then Mathieu (2006), proposed to take into account the plasticity mechanisms effects on fracture.

Our paper deals with the effect of these plasticity mechanisms. For this purpose, the local mechanical fields are first computed (Libert, 2007). The results enable the evaluation of the probability of cleavage fracture of a representative volume, for different temperatures (starting from the lowest shelf to the beginning of the brittle–ductile transition temperature regime) and for two constraint conditions.

Section 2 is devoted to the description of the polycrystal model equations introducing the change of plasticity mechanisms with temperature. Section 3 corresponds to an application of the model to the bainitic microstructure submitted to tri-axial loading. Section 4 deals with the mechanical behavior, the determination of material parameters, the meshing and boundary conditions. As a result, the evolution of the local mechanical fields is given. Section 5 is devoted to the computation of the probability of rupture from the local stress histogram. Section 6 is a first step to determine the Beremin's criterion within an aggregate containing a defect such as carbide. Section 7 closes the paper with a discussion and a conclusion.

2. Polycrystal model of the BCC behavior at low and high temperatures

At the grain scale (micrometer scale), the behavior of each grain is assumed similar to a single crystal behavior. The used single crystal plasticity model was developed within the framework of large transformations (with small elastic distortion and large

lattice rotation) proposed by Peirce et al. (1983), then Teodosi et al. (1993) and implemented in Abaqus® FE code, using a FORTRAN user Subroutine UMAT.

An unified constitutive description of the mechanical behavior for BCC materials is proposed, within the framework of the classical theory of thermally activated dislocations. The description spans over a large temperature interval on both sides of the mechanism transition temperature T_0 . It is worth noting that the transition temperature for brittle–ductile behavior T_d differs from T_0 , but belongs to the analyzed temperature interval.

2.1. Constitutive law

The model takes into account crystallographic glide and resulting lattice rotation. For BCC structure, glide is expected to occur on the 24 slip systems $\{110\}\langle 111 \rangle$ and $\{112\}\langle 111 \rangle$. The chosen viscoplastic law can describe the competition between lattice friction and forest hardening. According to Kubin et al. (1978), Rauch (1993) and Tang et al. (1998), the slip rate on a given slip system, hereafter named (s), is given by

$$\dot{\gamma}^s = \dot{\gamma}_0 \exp \left[-\frac{\Delta G(\tau_{eff}^s)}{k_B T} \right] \frac{\tau^s}{|\tau^s|} \quad (1)$$

where $\Delta G(\tau_{eff}^s)$ is the activation energy, which is a function of the effective shear stress τ_{eff}^s . k_B is the Boltzmann's constant and T is the absolute temperature. τ^s and $\dot{\gamma}_0$ are the resolved shear stress on system (s) and the reference shear rate respectively.

When $T < T_0$, the reduced mobility of the screw dislocations controls the plasticity. The proposed flow law takes into account the crossing of Peierls valleys by double kink mechanisms. The shear rate $\dot{\gamma}$ depends on the geometry of segments of screw dislocations. The activation energy is given by the phenomenological description proposed by Kocks (1976):

$$\Delta G(\tau_{eff}^s) = \Delta G_0 \left(1 - \left(\frac{\langle \tau_{eff}^s \rangle}{\tau_R} \right)^p \right)^q \quad (2)$$

Above p and q exponents are describing the energy associated to the Peierls barriers. In Eq. (2), τ_R is the effective stress to supply, in order to create a double kink at $T = 0\text{ K}$, when the contribution of the thermal activation is strictly equal to zero. The brackets $\langle \cdot \rangle$ are the McCauley brackets ($\langle u \rangle = u$ if $u > 0$, $\langle u \rangle = 0$ otherwise). This description implicitly assumes that the glide of dislocations on a system (s) is only activated when τ_{eff}^s is larger than zero.

2.2. Hardening law

The strain hardening evolution with temperature depends on interactions between mobile dislocations and lattice friction and/or forest dislocations. Lattice friction generates short range stresses described by the effective shear stress τ_{eff}^s . The shear stresses τ_{int}^s and τ_0 , stand for interaction between mobile dislocations and dislocations piercing their slip planes or precipitates and lattice friction respectively. Thus, the yield stress required to activate the glide system (s) is equal to the sum of these three contributions:

$$|\tau^s| = \tau_0 + \tau_{eff}^s + \tau_{int}^s \quad (3)$$

By considering a segment of a screw dislocation (pinned by two obstacles) submitted to the lattice friction and to the interactions with precipitates (τ_0), Rauch (1993) proposed an expression of the internal stress:

$$\tau_{int}^s = \frac{(\mu b)^2 \sum_{u=1,24} a^{su} \rho^u}{|\tau^s - \tau_0|} \quad (4)$$

a^{su} is a component of the interaction matrix proposed by Franciosi (1983), bound to the interaction energy between the systems (s) and (u) (self and latent hardening). It is worth noting that a^{su} depends on the deformation ratio. In this paper, we use the asymptotic value which corresponds to a deformation up to 0.5%. ρ^u is the dislocation density on glide system (u). Introducing expression (3) in (4) and solving the resulting equation, one obtains:

$$|\tau^s| = \tau_0^s + \frac{\tau_{eff}^s}{2} + \frac{1}{2} \sqrt{(\tau_{eff}^s)^2 + 4(\mu b)^2 \sum_u a^{su} \rho^u} \quad (5)$$

The general expression of the hardening law (5) is appropriate to describe a continuous evolution of the shear stress with temperature. In the case of low temperature behavior ($T < T_0$), plasticity is governed by the reduced mobility of the screw dislocations and τ_{int} can be neglected, compared to τ_{eff} . Eq. (5) leads to

$$|\tau^s| = \tau_0 + \tau_{eff}^s + \frac{(\mu b)^2 \sum_{u=1,24} a^{su} \rho^u}{\tau_{eff}^s} \quad (6)$$

In the case of high temperature, ($T > T_0$), plasticity depends on forest hardening and τ_{eff} is small compared the two other terms. Eq. (5) leads to

$$|\tau^s| = \tau_0^s + \mu b \sqrt{\sum_{u=1 \text{ to } 24} a^{su} \rho^u} \quad (7)$$

At low temperature, plastic deformation occurs according to two non equivalent slip systems $\{111\}\{110\}$ and $\{111\}\{112\}$. The gap between the two shear stresses $\tau_0^{\{110\}}$ and $\tau_0^{\{112\}}$ is not yet well understood (Keh, 1964; Spitzig and Keh, 1970a,b). We assume that $\tau_0^{\{110\}}$ is a constant and that $\tau_0^{\{112\}}$ depends on temperature, according to Eqs. (8a) and (8b):

$$\tau_0^{\{110\}} = \tau_0 \quad (8a)$$

$$\tau_0^{\{112\}} = \tau_0 + f(T) \quad (8b)$$

The function $f(T)$ will be identified in the next section.

Note: the carbides size being less than 300 nm, carbides cannot be considered individually in this micrometer scale investigation. Their impact on plasticity is then averaged through $\tau_0 + \tau_{int}^s$ for low temperatures and τ_0 for high temperatures. For low temperature, τ_0 is considered constant and τ_{int}^s is temperature dependant. With this assumption, τ_0 has the same value for high and low temperature.

2.3. Dislocations evolution law

The dislocation evolution law is a generalization of the relation proposed by Estrin and Mecking (1984). Eq. (9) describes the evolution of the 24 dislocation densities with strain for each slip system:

$$\dot{\rho}^s = \frac{|\dot{\gamma}^s|}{b} \left[\frac{1}{D_{grain}} + \frac{\sqrt{\sum_{u \neq s} \rho^u}}{K(T)} - g_c(T) \rho^s \right] \quad (9)$$

b is the norm of the Burgers vector.

This equation is derived from the balance between dislocation accumulation (Orowan's relationship) and dislocation annihilation rate. $K(T)/\sqrt{\sum_{u \neq s} \rho^u}$ is the dislocations mean free path. This term increases with decreasing temperature because the evolution of dislocation densities is smaller for low temperature. Consequently, we assume that $K(T)$ increases with decreasing temperature. D_{grain} is the mean lath packet thickness. This term plays a part only in case of low initial dislocation density. The annihilation of dislocations is controlled by the g_c parameter, which temperature dependence is expressed here by an Arrhenius law.

$$g_c(T) = g_{c0} \exp \left[-\frac{E_{gc}}{k_B T} \right] \quad (10)$$

g_c and E_{gc} are two material dependent parameters.

According to Eq. (9), two dislocations of the same system (s) may annihilate each other as soon as they are localized at a distance smaller than g_c .

3. Model application to bainitic steel mechanical behavior in the brittle–ductile temperature range

The model of local mechanical stresses requires an accurate knowledge of the microstructure and the identification of the material parameters in the temperature range $[-196^\circ\text{C}$ to $25^\circ\text{C}]$, which corresponds to the brittle–ductile transition of bainite.

At low temperature, plastic deformation occurs through double kink formation which requires large resolved stresses. Kubin et al. (1978), proposed an expression of formation of double kink frequency bound to the strain-rate equations through:

$$\dot{\epsilon} = \dot{\epsilon}_0 \exp \left[-\frac{\Delta G(\tau_{eff})}{k_B T} \right] \quad (11)$$

$\dot{\epsilon}_0$ is a term depending on the mobile dislocation densities.

3.1. Microstructures and mechanical characterization

The determination of the model parameters is based on different macroscopical mechanical tests as well as microstructure analysis.

3.1.1. Microstructure analysis

The bainitic microstructure is obtained from an ingot ($16 \times 200 \times 300$ mm) of A508C13 steel by an austenitization process at 1150°C . The material is then air quenched at 0.4°C/s . The specimens are tempered at 610°C during 20 h. The chemical composition of the steel is given in Table 1.

The bainite microstructure is characterized by Electron Back Scattering Diffraction technique (Fig. 1). The initial density of dislocation is estimated to $\rho_0 = 10^{14} \text{ m}^{-2}$ using Transmission Electronic Microscope (TEM). The bainitic microstructure is not textured.

3.1.2. Mechanical characterization

Cylindrical tensile specimens (3 mm in diameter and with $L_0 = 15$ mm initial gauge length) were deformed in a ZWICK machine at four temperatures ($T = 25^\circ\text{C}$, -90°C , -150°C and -196°C). Tests were carried out under displacement control at a $\dot{\epsilon} = 5 \times 10^{-3} \text{ s}^{-1}$ constant rate. Uniaxial strain was measured using a calibrated extensometer. Samples were maintained at the involved testing temperature in a temperature controlled chamber.

Fig. 2 shows conventional tensile stress/strain curves for bainitic microstructures at different temperatures ranging from -196°C to 25°C . Tensile data are given in terms of nominal stress $\sigma = F/S_0$ and of strain $\epsilon = (L - L_0)/L_0$. S_0 is the initial cross sectional area of the samples.

We determined the activation energy ΔG for the studied steel through the combination of strain rate jump tests performed at different temperature and temperature jump tests at constant strain rates. These tests were performed on different specimens (4 mm

Table 1
Chemical composition of A508C13 steel.

C	Mn	Si	Cr	Ni	Mo	S	P	Cu	Al
0.25	1.29	0.23	<0.05	0.72	0.49	0.008	0.014	0.03	0.035

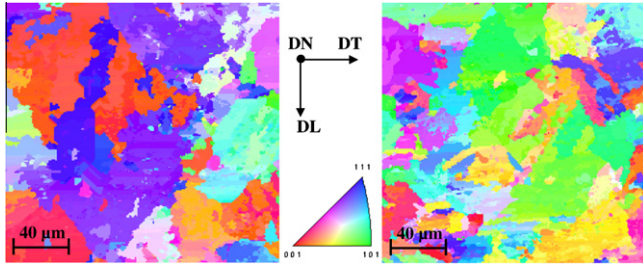


Fig. 1. Bainite microstructures A and B, orientation mapping of the normal (DN) to the sample. The orientations of the normal in the different grains are depicted by the different colors of the standard triangle. The boundary conditions are applied according to the directions DL and DT. (For interpretation of the references to colour in this figure legend, the reader is referred to the web version of this article.)

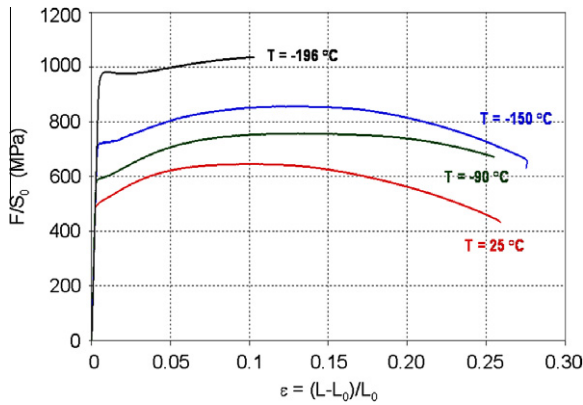


Fig. 2. Tensile curves at different temperature.

diameter cylindrical specimens with a 17 mm gauge length) with an INSTRON servo-hydraulic machine. Errors in the measured deformation are less than 1%.

3.1.3. Strain rate change tests

A change of strain rate from $5 \times 10^{-3} \text{ s}^{-1}$ to $5 \times 10^{-4} \text{ s}^{-1}$ is applied for each increase of 2.5% of the true plastic strain. This is achieved at -150°C , -90°C , -60°C and 25°C . Rational stress-strain curves are presented in Fig. 3a. Each curve corresponds to an average result corresponding to several identical tests. The dispersion on the Cauchy stress jump $\Delta\sigma$ is less than 20 MPa. The $\Delta\sigma$ amplitude gap is found to decrease with increasing temperature.

3.1.4. Temperature change tests

Temperature jumps from $T_1 = -150^\circ\text{C}$ to $T_2 = -196^\circ\text{C}$ (liquid nitrogen) were realized and their effect on stress-strain curves at constant strain rate was studied. The amplitude of the gap $\Delta\sigma$ appeared to be constant regardless of the strain amplitude (Fig. 3b).

3.2. Determination of activation energy and activation volume

Thermally activated plasticity mechanisms are characterized by the so called activation volume V^* and the activation energy ΔG . V^* and ΔG are deduced from the experimental curves presented in Fig. 3a and b, through Eqs. (12) and (13)

$$V^* = \frac{k_B T}{\Delta\sigma} \Delta \ln \dot{\epsilon} \quad (12)$$

For a temperature gap $\Delta T = T_2 - T_1$, the variation ΔG is given by (13):

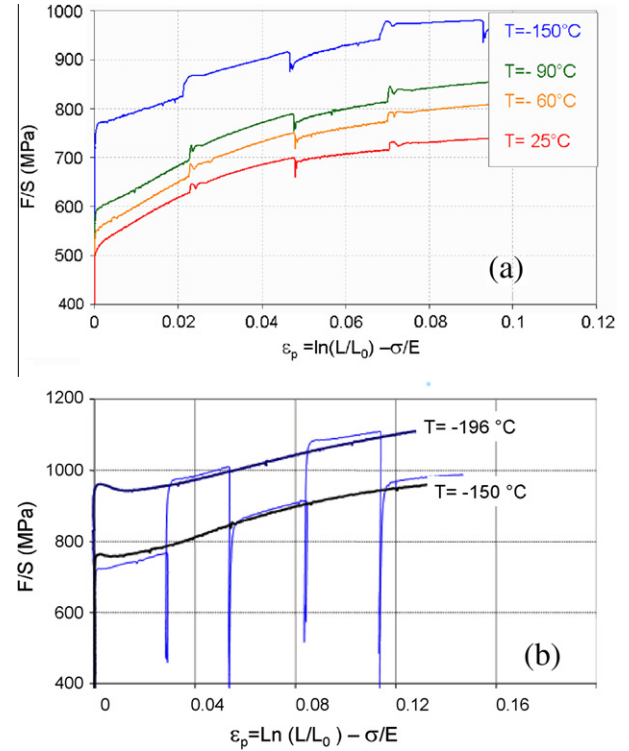


Fig. 3. Strain rate jump tests (a) and temperature jump tests (b).

$$\Delta G = k_B (T_1)^2 \left(\frac{\Delta \ln \dot{\epsilon}}{\Delta \sigma} \right)_T \left(\frac{\Delta \sigma}{\Delta T} \right)_\epsilon \quad (13)$$

The identification results are given in Table 2.

For $T < T_0$, the obtained computed value of the activation energy is $\Delta G = 0.41 \text{ eV}$. This value is consistent with literature devoted to low carbon steels and pure iron (Kocks et al., 1975; Kocks, 1976; Astié et al., 1981; Nemat-Nasser et al., 1998; Tang et al., 1998). For bainitic microstructure presenting low carbide density, we think that the size of microstructure does not strongly modify the plasticity mechanisms of the ferrite. According to our results, thermal activation is then only bound to the ferrite behavior. At high temperature, $T > T_0$, $\Delta G(\tau_{eff}) \approx \Delta G_0$ and therefore these experiments enable us to identify ΔG_0 material parameter, namely $\Delta G_0 = 1 \text{ eV}$.

3.3. Model parameters determination

The model depends on 12 material parameters $\dot{\gamma}_0$, τ_R , p , q , τ_0 , a^{su} , $K(25^\circ\text{C})$, $K(-60^\circ\text{C})$, $K(-90^\circ\text{C})$, $K(-150^\circ\text{C})$, $K(-196^\circ\text{C})$, g_{c0} , E_{gc} . Initial dislocation density ρ_0 and activation energy ΔG_0 are derived from experimental data. D_{grain} is directly measured and corresponds to twice the mean thickness of lath packets. The other parameters are obtained by an inverse method. The above mentioned $K(T)$ parameter, being strongly dependent of lattice friction, must be determined for the five studied temperatures (-196°C , -150°C , -90°C , -60°C , 25°C). The parameters g_{c0} and E_{gc} are computed assuming that $g_c = 0.7 \text{ nm}$ at -196°C (corresponding

Table 2
Activation volume and activation energy deduced from experiments.

$T (^\circ\text{C})$	25	-60	-90	-150	-196
$V^* (\times b^3)$	55	25	20	9	≈ 9
$\Delta G (\text{eV})$	1.00	\times	\times	0.41	≈ 0.4

to three times the norm of Burgers vector) and that $g_c = 8$ nm at 25 °C.

3.3.1. Parameters determination process

This process is supported by the experimental tensile curves at different temperatures. Using the SiDoLo software (Cailletaud and Pilvin, 1994), experimental tensile curves are compared for different sets of parameters to the computed tensile curves obtained from an aggregate constituted by a cube representing 512 crystal-line orientations with a cube of size $2 \times 2 \times 2 \mu\text{m}^3$ finite element for each orientation. The finite element meshing is constituted by 8 nodes cubic elements with reduced integration (C3D8R). Fig. 4 shows experimental and computed tensile curves. We note that the computed hardening slopes fit with experimental ones, when strain is higher than 5%. As expected, the model does not predict Lüders phenomena due to different elements of the alloy. Involved optimized parameters are given in Table 3.

The elastic moduli of the cubic symmetric material are taken equal to $C_{11} = 275.2$ GPa, $C_{12} = 112.4$ GPa, $C_{44} = 81.4$ GPa. These values are chosen to represent an isotropic elastic behavior of the material both at the microscopic and macroscopic scales. Heterogeneities due to local anisotropic elastic behavior are thus not taken into account in the model.

3.4. Aggregates and boundary conditions

Two investigated aggregates $210 \times 201 \times 3 \mu\text{m}^3$ are generated from EBSD experiments. They are constituted by 3 identical layers, leading to a representative volume of $(50 \mu\text{m})^3$. The meshing contains 126,000 elements (C3D8R elements, 8-node linear with reduced integration).

Three Euler's angles (given by EBSD) are allocated to each element ($1 \mu\text{m}^3$) of the meshing depicting a part of a grain.

In order to determine the distribution of local mechanical fields prevailing at the crack tip of Compact Tension (CT) specimens, the

aggregates are submitted to plane deformation and different tri-axial ratios. As shown in Figs. 8–10 of Section 4.2, uniform stress Σ_1 and are directly applied to the surfaces normal to \vec{E}_2 and \vec{E}_1 , respectively, such as $\Sigma_1 = k\Sigma_2$, where k is a given proportionality factor. The displacement of the two faces normal to \vec{E}_3 is kept equal to zero, leading to plane strain conditions. In the plastic stage, $\Sigma_3 = 1/2(k+1)\Sigma_2$ and the average value of component E_{33} is equal to zero. The tri-axial ratio χ of the loading applied to the aggregate is given by: $\chi = (\sigma_{11} + \sigma_{22} + \sigma_{33})/(3\langle\sigma_{Mises}\rangle)$, where the $\langle \rangle$ brackets correspond to the mean value on the whole aggregate. Taking into account the above expressions of Σ_2 and Σ_3 , χ becomes: $\chi = (\sqrt{3}k+1)/(\sqrt{3}k-1)$.

4. Evolution of the local stress field with temperature and tri-axial ratio

We respectively name E and Σ the macroscopic strain and stress fields and ε and σ the local strain and stress fields in the meshing elements.

For four temperatures $T = -60$ °C, -90 °C, -150 °C and -196 °C, two macroscopic tri-axial ratios (namely $\chi = 1.5$ and $\chi = 2.5$) were considered. The local strain and stress fields as well as the mean maximal principal stress $\langle\sigma_1\rangle$ were computed. The average strain component $\langle\varepsilon_{11}\rangle$ (i.e. the average strain on all elements of an aggregate) and the equivalent strain ($\varepsilon_{equ} = \sqrt{(\frac{2}{3}\varepsilon:\varepsilon)}$) were also evaluated.

4.1. Strain and stress distributions

We name $\langle\sigma_1\rangle$ the mean principal stress on the whole aggregate computed from the local values of the maximum principal stress in each element of the aggregate. $\langle\sigma_1\rangle$ is equal to the applied macroscopic principal stress. For a given χ , the distribution curves of local maximum principal stress move towards larger values for decreasing temperature. We also notice an alteration of the peak

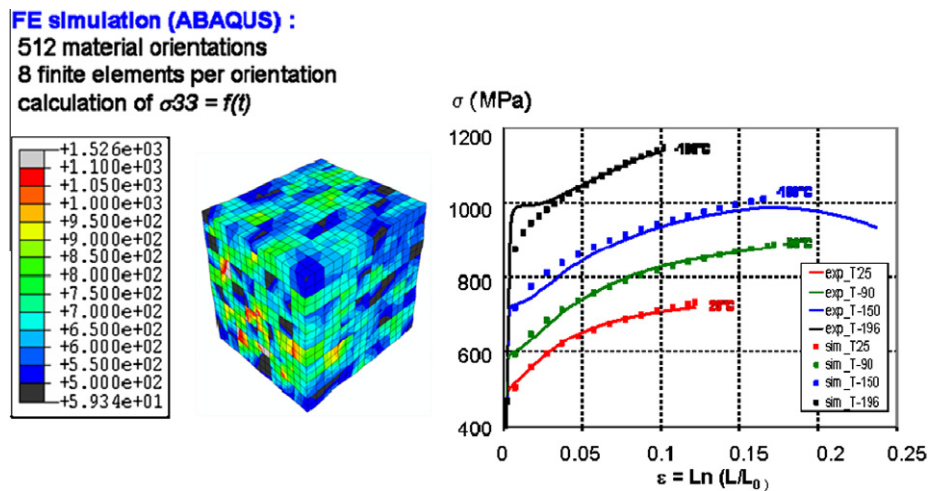


Fig. 4. Sketch of parameters determination method from comparison of FE simulation (512 material orientations, 8 elements per orientation) and experimental tensile curves. (Dashed pots simulation, Continuous lines: experimental results.)

Table 3
Material parameters of the model.

$\dot{\gamma}_0$ (s^{-1})	ΔG_0 (eV)	τ_R (MPa)	p	q	τ_0 (MPa)	a^{su}	D_{grain} (μm)
10^6	1.00	498	0.283	1.17	88.9	0.251	2.5
ρ_0 (m^{-2})	K (25 °C)	K (−90 °C)	K (−150 °C)	K (−196 °C)	g_{c0} (nm)	E_{gc} (eV)	
10^{14}	35.6	63.8	323.1	449.9	18.6	2.17×10^{-2}	

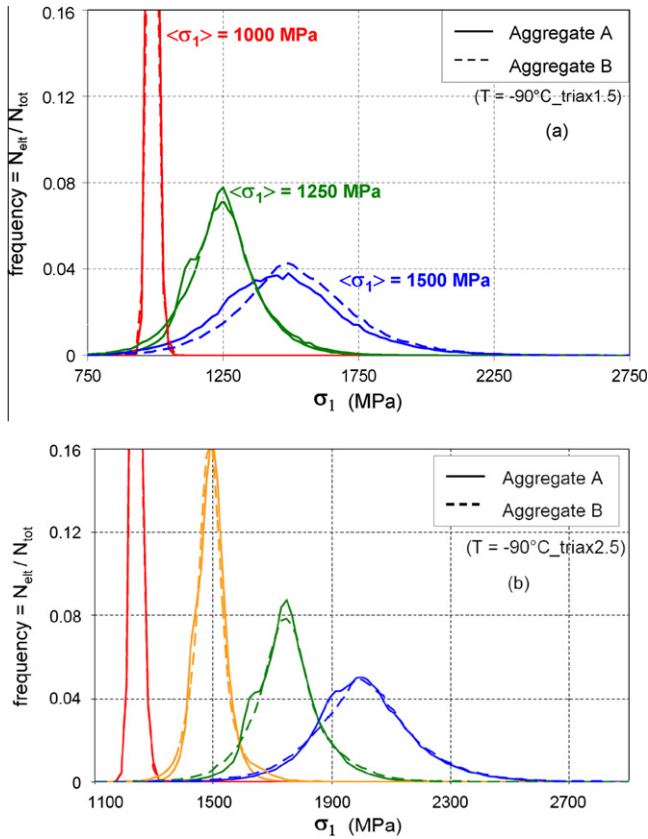


Fig. 5. Principal maximum stresses distributions for increasing average principal stress for aggregates A and B, for $T = -90^\circ\text{C}$. (a) $\chi = 1.5$; (b) $\chi = 2.5$.

shape (see Figs. 5 and 6). Such moves are partly explained by the growth of the yield point with decreasing temperature. Considering that the heterogeneity of the σ_1 distribution is given by the width at mid height of the curves, we point out that:

- For a given couple (T, χ) , the heterogeneities increase with increasing $\langle\sigma_1\rangle$ (Figs. 5 and 6).
- For a given couple $(T, \langle\sigma_1\rangle)$ the increasing of χ leads to a more homogeneous pattern (Figs. 5a, 5b, 6a and 6b).
- For a given couple $(\chi, \langle\sigma_1\rangle)$, the stress heterogeneity increases with increasing temperature (Fig. 7).

The two aggregates (referred as aggregate A and aggregate B) exhibiting the same distribution curves, as shown in Fig. 5, we assume that the two chosen aggregates are representative of the bainitic microstructure. Therefore, only curves about aggregate A are given in Fig. 7.

Table 4 gives the average of the equivalent strain corresponding to the average of the principal stress. We note that for equivalent principal stress conditions, deformation increases with increasing temperature.

4.2. Stress and strain maps

For two loading tri-axial ratios, Figs. 8–10 show the computed maps of the equivalent strain and of the principal stress distributions within aggregate microstructure at -90°C , -150°C and -196°C , respectively. For the sake of a better display of the maps, we must mention that we do not use the same scale for a given color in the different maps. The indicated largest value of maximal principal stress corresponds to the value beyond which the strain localization is so large that we would probably have a sample rup-

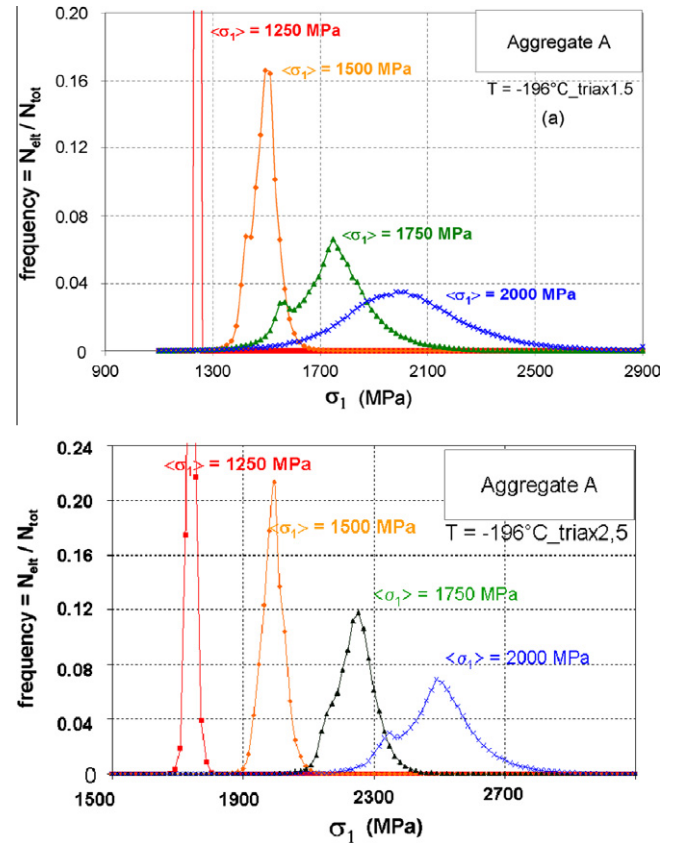


Fig. 6. Principal maximum stresses distribution for increasing average principal stress for aggregate A, for $T = -196^\circ\text{C}$. (a) $\chi = 1.5$; (b) $\chi = 2.5$.

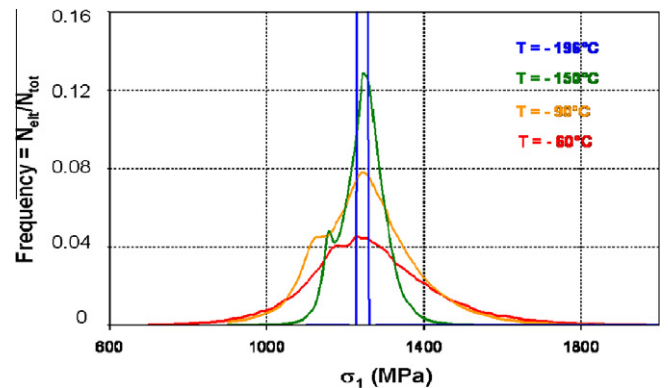


Fig. 7. Maximal principal stress distribution σ_1 for different temperatures T (aggregate A, $\langle\sigma_1\rangle = 1250$ MPa, $\chi = 1.5$).

ture. Let us point out that the strain and stress distributions are different. Equivalent strain is localized in thin bands, which are tilted of about $\pm 45^\circ$ with the sample axes. For $\chi = 2.5$ and $T = -90^\circ\text{C}$ the maximum value of the local equivalent strain reaches 31%, for an average strain $\langle\epsilon_{\text{equ}}\rangle = 6.4$. For -196°C , the maximum of the local equivalent strain value reaches only 7% for $\langle\epsilon_{\text{equ}}\rangle = 2.5$. The maximal principal stress is located close to some grains boundaries. We also notice some large values of stress between strain localization bands.

According to these results, for low temperatures and large tri-axial loading ratios, large stresses can induce damage at grain boundaries. This effect is enforced by the segregation of different chemical elements.

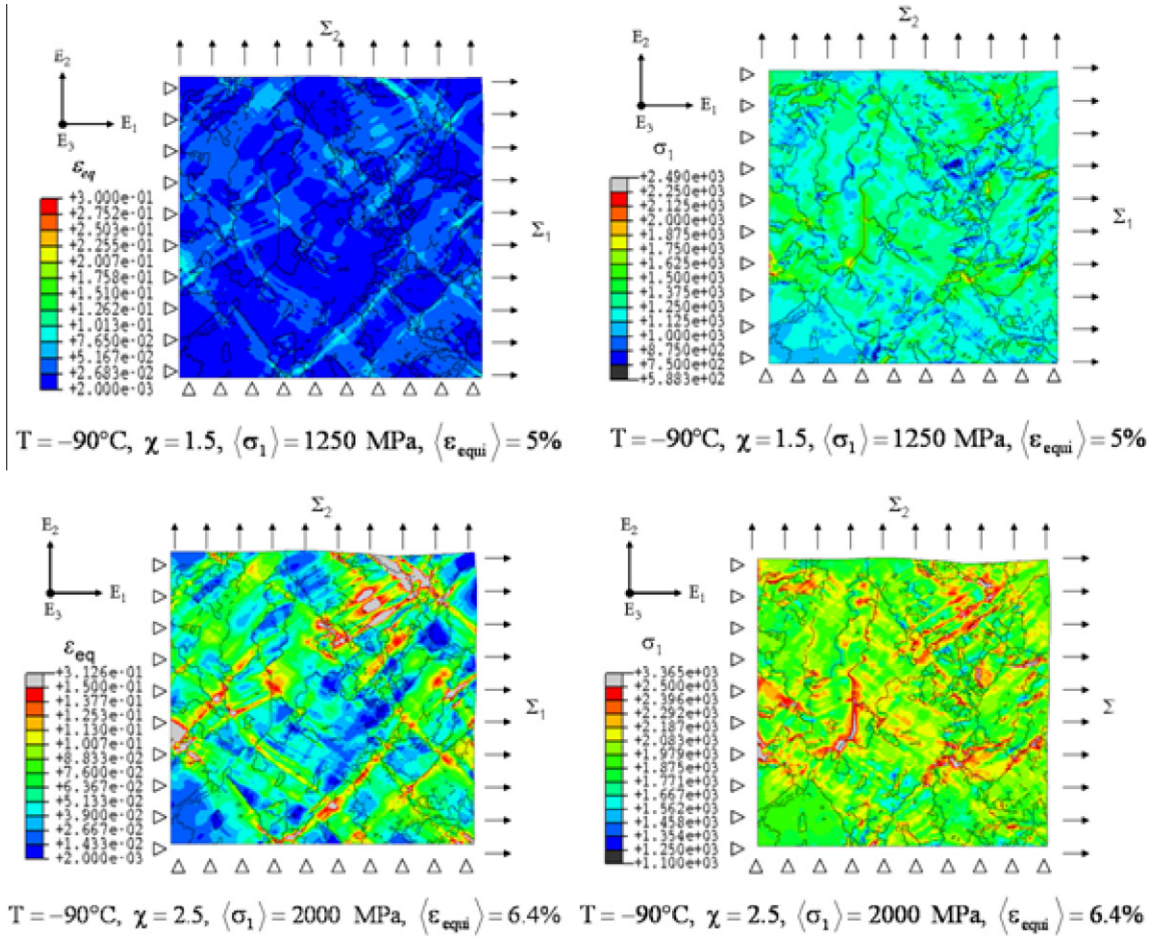


Fig. 8. Equivalent strain and maximal principal stress distributions within the aggregate microstructure. $T = -90^\circ\text{C}$, $\chi = 1.5$ and $\chi = 2.5$.

Let us sum up our main results:

- Whatever the temperature and the tri-axial loading, we observe that the strain patterns present the same global aspect, showing localization bands.
- For decreasing temperatures and increasing tri-axial loading ratio, the aggregate plastic deformation becomes uneasy, owing to the low mobility of the screw dislocations. Thus, the local principal stress increases close to grain boundaries where the plastic incompatibilities cannot be relaxed by plastic glide activation. This may explain the differences between strain and stress maps which are specific to tri-axial loading.
- As soon as the temperature decreases, the strain and stress patterns become more homogeneous.

5. Application to fracture probability of the aggregate

5.1. Stress distributions and fracture probability

It is assumed that micro-cracks are nucleated at carbide sites as soon as plastic slip is active. The fracture propagates from micro-cracks through the lath packets when the critical stress σ_c is reached. According to classical theory of cleavage, this critical stress depends on the micro-crack size and consequently on the carbide size:

$$\sigma_c = \sqrt{\frac{2E\gamma_s}{\pi(1-\nu^2)r_c}} \quad (14)$$

In the Griffith criterion, r_c is the considered size defect, E the Young modulus and γ_s the surface energy. The weakest link hypothesis assumes that the fracture of the considered amount of steel i.e. the fracture occurs when, at least, one volume containing carbides is broken. This volume is called a cell.

Local stresses are computed for different couples of stress tri-axiality ratio χ and temperature (Libert, 2007). The computed fields present large heterogeneities, as given by the histograms of the local maximum principal stress σ_1 for different loading steps (Figs. 5 and 6).

It is assumed that extreme values of the maximum principal stress distributions can be described by a statistical function of Gumbel: the probability for the local principal stress σ_1 to be lower than a given stress σ is

$$P(\sigma) = P(\sigma_1 < \sigma) = \exp \left[-\exp \left(-\frac{\sigma - A}{B} \right) \right] \quad (15)$$

Therefore, the probability to have $\sigma_{\text{cell}} > \sigma_c$ i.e. the probability of fracture of the i th cell is given by

$$P(\sigma_{\text{cell}}^i > \sigma_c) = P_R^i(\sigma_c) = 1 - \exp \left[-\frac{\sigma_c - A}{B} \right] \quad (16)$$

For a representative volume V_0 composed of N cells, initiation of cleavage may occur independently in any cell and has the same probability of occurrence. Then the probability of fracture of V_0 is

$$P_{R0}(\sigma_c) = 1 - \left[1 - P_R^i(\sigma_c) \right]^N \quad (17)$$

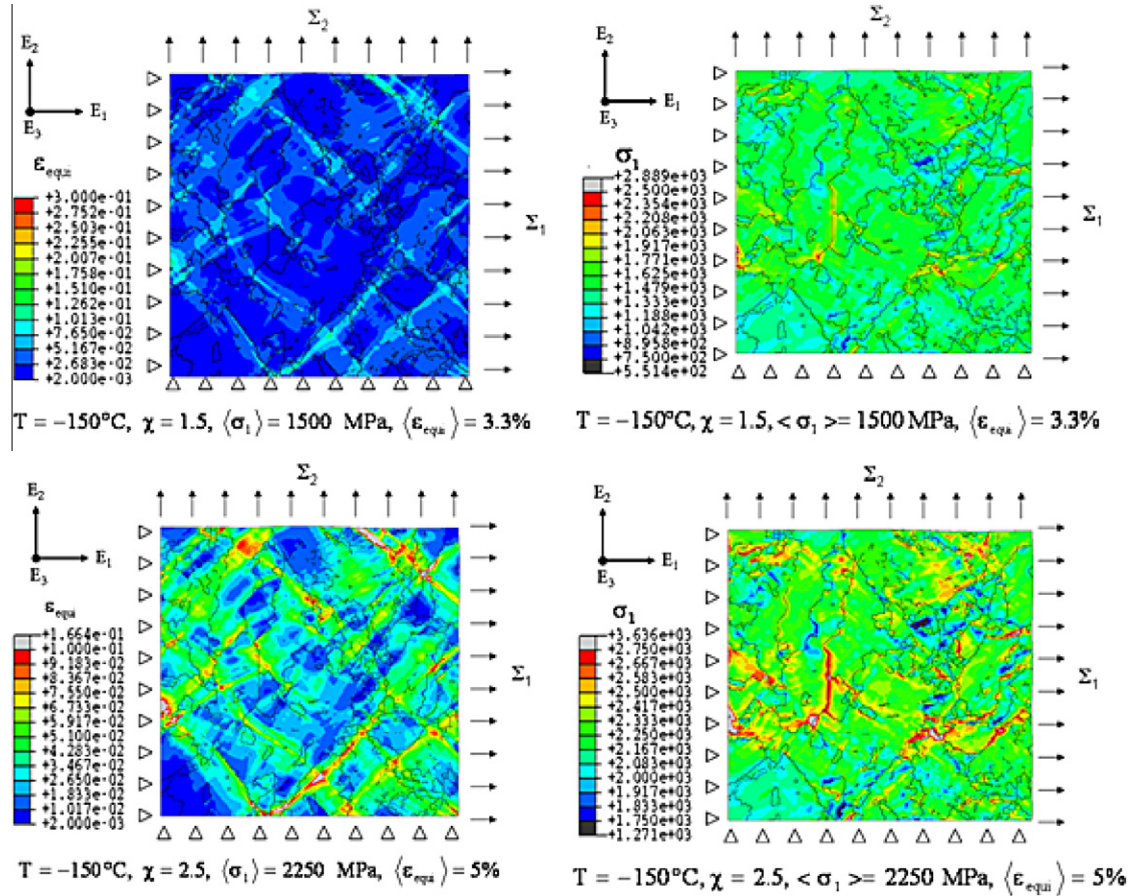


Fig. 9. Equivalent strain and maximal principal stress distributions within the aggregate microstructure. $T = -150^\circ\text{C}$, $\chi = 1.5$ and $\chi = 2.5$.

From Eqs. (16) and (17), the expression of the fracture probability of the representative volume V_0 is derived:

$$P_{R0}(\sigma_c) = 1 - \left[\exp \left[- \exp \left(- \frac{\sigma_c - A}{B} \right) \right] \right]^N \quad (18)$$

5.2. Determination of parameters of the stress distribution

The parameters of the extreme values of the maximum principal stress are determined using Libert's simulation results. For $\chi = 2.5$, $T = -196^\circ\text{C}$ the result of this determination process is plotted in (Fig. 11) for different values of $\langle\sigma_1\rangle$.

To identify A and B coefficients, a minimum value of 0.7 for the probability $P(\sigma > \sigma_1)$ is used, since only extreme stress values are involved. Fig. 12 presents the results obtained for $T = -196^\circ\text{C}$, $\chi = 2.5$, and different $\langle\sigma_1\rangle$ values.

The two parameters A and B are correlated with respect to the average maximum principal stress by (Fig. 13):

$$\langle\sigma_1\rangle = A - B\Gamma'(1) \quad \text{with } \Gamma'(1) = -0.577 \quad (19)$$

Fig. 14 shows that B is governed by the average von Mises stress linear law:

$$B = \alpha\langle\sigma_{\text{eq}}\rangle + \beta(T) \quad (20)$$

This expression is only valid for plasticity state and for $B > 0$.

We notice that α parameter weakly depends on temperature (see Table 5), whereas β parameter is a decreasing function of temperature. If the stress distribution is homogeneous, B tends towards zero. For a stress lower than the yield stress σ_Y , $B = 0$ and

$\sigma_Y = -\beta/\alpha$. Physically, B is a measure of the stress heterogeneity induced by the incompatibilities of the plastic strain.

Using Eqs. (19) and (20) in Eq. (18), the fracture probability of the representative volume V_0 is given by

$$P_{R0} = 1 - \left[\exp \left[- \exp \left(- \frac{\sigma_c - \langle\sigma_1\rangle}{\alpha\langle\sigma_{\text{eq}}\rangle + \beta(T)} + \Gamma'(1) \right) \right] \right]^N \quad (21)$$

The equivalent stress $\langle\sigma_{\text{eq}}\rangle$ is related to $\langle\sigma_1\rangle$ and χ , by

$$\langle\sigma_{\text{eq}}\rangle = \frac{\sqrt{3}(k-1)}{2k} \langle\sigma_1\rangle \quad \text{and} \quad k = \frac{\chi\sqrt{3}+1}{\chi\sqrt{3}-1}$$

The α and $\beta(T)$ tuning values of are reported in Table 5.

6. Effect of a carbide on rupture probability

In this section, within the frame of classical local approach to rupture (using the weakest link theory) we consider the aggregate as an elementary volume ($V_0 = (50 \mu\text{m})^3$) made of 125 cells (approximately corresponding to the number of bainitic laths packets in V_0).

Carbides being considered as major initiators of rupture (Tanguy et al., 2003, 2005), we introduce a constant carbide size (i.e. a constant micro-crack size) within the aggregate. This is equivalent to the introduction of a constant critical stress, enlightening the effect of heterogeneities of the local stress field on rupture probability.

Considering the Griffith's criterion (Eq. (14)), micro-crack propagation occurs for a 3700 MPa cleavage critical stress σ_c . The

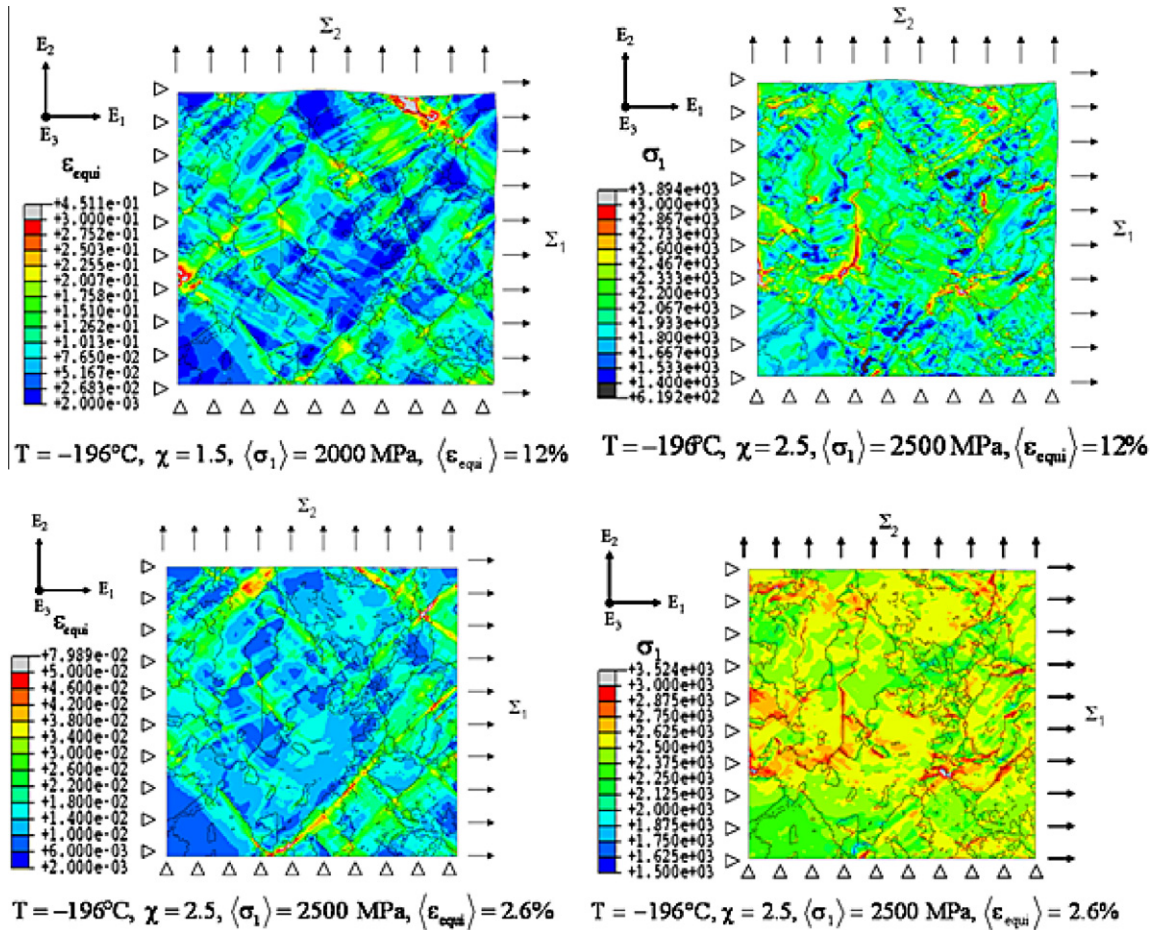


Fig. 10. Equivalent strain and maximal principal stress distributions within the aggregate microstructure. $T = -196^\circ\text{C}$, $\chi = 1.5$ and $\chi = 2.5$.

Table 4

Average of the principal stress and average equivalent strain computation.

T ($^\circ\text{C}$)	$\chi = 1.5$		$\chi = 2.5$	
	$\langle\sigma_1\rangle$ (MPa)	$\langle\epsilon_{\text{equi}}\rangle$ (%)	$\langle\sigma_1\rangle$ (MPa)	$\langle\epsilon_{\text{equi}}\rangle$ (%)
-196°C	2028	12.7	2505	2.6
-150°C	1512	3.3	1500	1.2
			2250	5.0
-90°C	1262	5	1501	3.4
	1481	20.9	2000	6.4
-60°C	1270	7.2	1504	5.1
			1763	7.7

surface energy is arbitrarily set to $\gamma_s = 2 \text{ J m}^{-2}$ and the defect size is set to $r_c = 0.052 \mu\text{m}$ (these two values being typical for the pressure vessel steels). The evolution of the fracture probability $P_{R0}(\langle\sigma_1\rangle)$ of the aggregate, versus the mean maximum principal stress, is then computed from Eq. (21) for different sets of T and χ .

For a stress tri-axiality ratio of 2.5, we find that P_{R0} is a decreasing function of the temperature (Fig. 15), since the flow stress is decreasing with temperature. However, let us note that the rupture probability scattering appears to increase with temperature.

For a constant $\langle\sigma_1\rangle$ value and a constant temperature, computations pointed out a decrease of stress field heterogeneities (corresponding to the width of the distribution) with increasing χ . Consequently, the scattering of the distributions of $\langle\sigma_1\rangle$ values at aggregate rupture (observed in Fig. 16) is the highest for the lowest values of stress tri-axiality.

6.1. Comparison to Beremin's model

For low alloyed steels, the Beremin model (Beremin, 1983) describes the scattering of the cleavage fracture stress. For the representative volume (V_0), the fracture probability corresponds to the probability of finding the random variable σ_c lower than the mean principal stress $\langle\sigma_1\rangle$:

$$P_{R0} = P(\sigma_c < \langle\sigma_1\rangle) = 1 - \exp\left(-\frac{\langle\sigma_1\rangle}{\sigma_u}\right)^m \quad (22)$$

where:

- σ_u is the stress leading to a rupture probability of 63%,
- m is a coefficient depending on material characteristics.

σ_u and m were determined by several authors on pressure vessel steels, using macroscopic tests performed on notched and CT

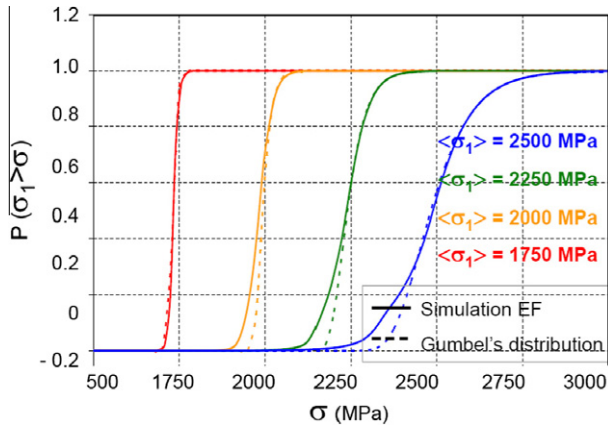


Fig. 11. Determination of Gumbel functions from the distributions curves of σ_1 ($T = -196^\circ\text{C}$ and $\chi = 2.5$).

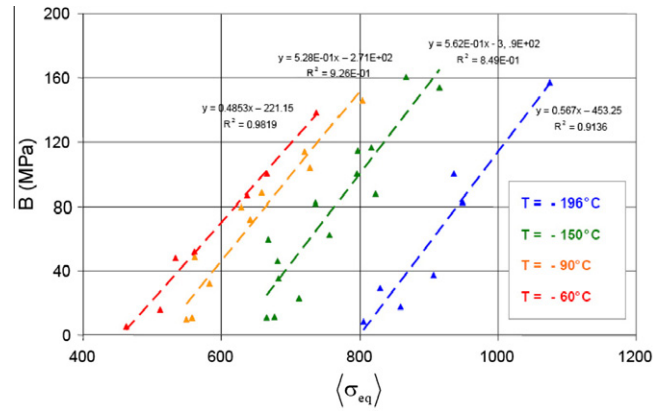


Fig. 14. Evolution of B with $\langle\sigma_{eq}\rangle$.

Table 5

Determination of α and β parameters from the linear function ($B = \alpha(\sigma_{eq}) + \beta$).

$T(^{\circ}\text{C})$	α	β
-196	0.567	-453
-150	0.562	-349
-90	0.528	-271
-60	0.485	-221

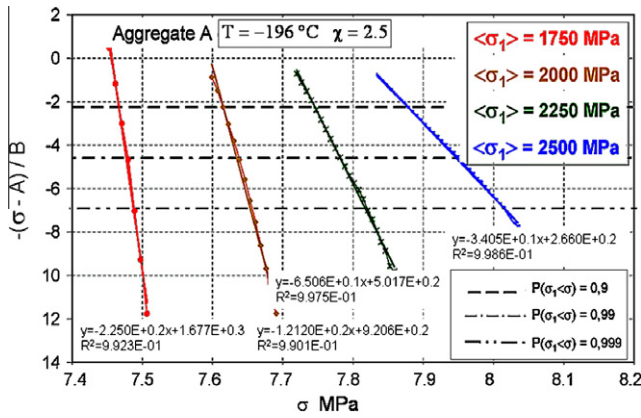


Fig. 12. Gumbel function evolution versus stress for the aggregate ($T = -196^\circ\text{C}$, $\chi = 2.5$).

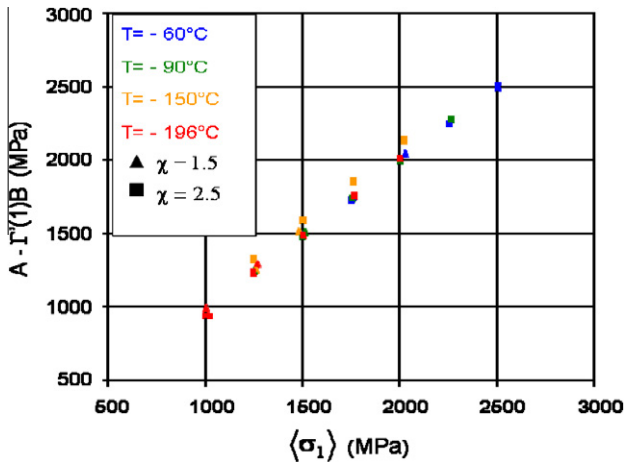


Fig. 13. Correlation between the two parameters A and B .

type specimens. We use here the typical characterization made by Carassou (1999): m values ranges between 12 and 28 and σ_u values from 2860 to 3140 MPa.

In comparison with Beremin model, we consider two extreme cases:

- $T = -60^\circ\text{C}$ and $\chi = 1.5$ leading to large dispersion of $P_{R0}(\langle\sigma_1\rangle)$.
- $T = -196^\circ\text{C}$ and $\chi = 2.5$ leading to small dispersion of $P_{R0}(\langle\sigma_1\rangle)$.

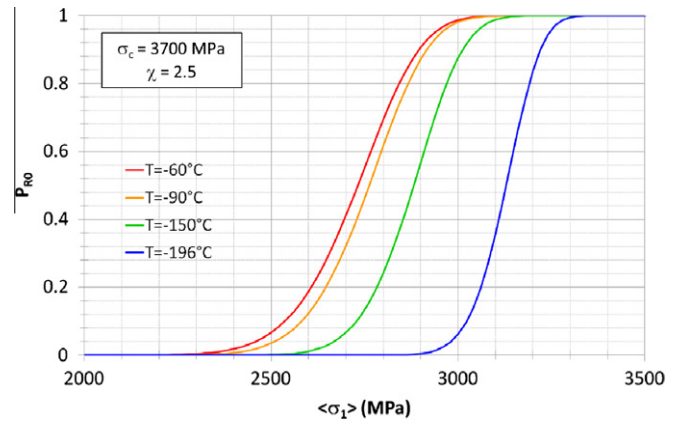


Fig. 15. Rupture probabilities versus the average principal stress for 4 temperatures.

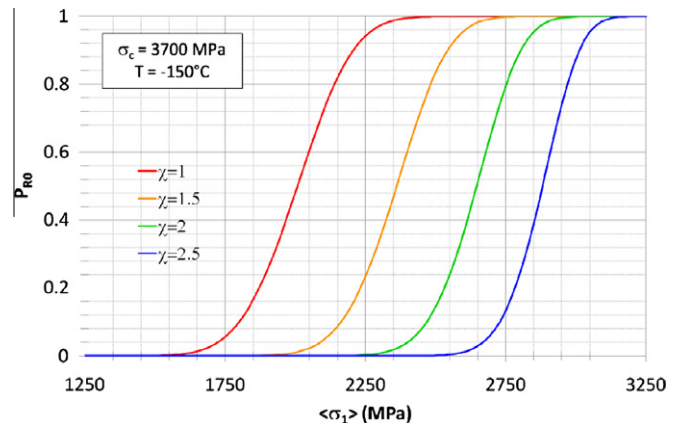


Fig. 16. Rupture probability $P_{R0}(\langle\sigma_1\rangle)$ versus the mean principal stress for different χ values.

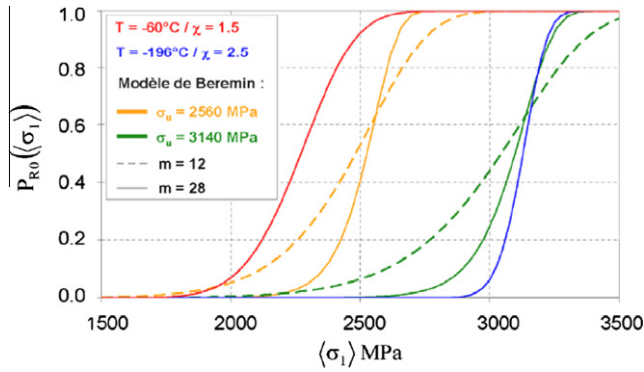


Fig. 17. Comparison of the extreme distributions of $P_{R0}(\sigma_1)$ for Beremin's model and for our model.

The two resulting curves are plotted in Fig. 17 and are compared to the Beremin model predictions.

The comparison shows that the Beremin's model is approximately included within the two extreme cases of our model. This shows that the scattering in fracture stress induced by stress heterogeneity is of the same order of magnitude as the experimental scattering. For a given temperature, the inhomogeneities of the local mechanical fields lead to sharpen the scattering of the rupture probability.

In classical local approach to rupture, scattering of the cleavage fracture stress occurs owing to the distribution of carbide sizes (Beremin, 1983). An extension of the above computation is performed by using the carbide size distribution identified by Lee et al. (2002):

$$P(r > r_c) = \exp \left[- \left(\frac{2r_c - a}{b} \right)^m \right] \quad (23)$$

where $a = 0.00917$, $b = 0.10158$ and $m = 1.192$ for bainitic steels.

This approach will be extended to a structure containing several elementary volumes, each of them containing an actual carbide size distribution.

Note that fracture can be also studied as a function of applied strain (instead of the principal stress) by integrating dP_{R0} with respect to r_c :

$$P_{R0} = 1 - \left\{ 1 - \int_{a/2}^{\infty} f(r_c) \left[1 - \exp \left(\exp \left(- \frac{\sigma_c(r_c) - \langle \sigma_1 \rangle}{\alpha'(T, \chi) \langle \sigma_1 \rangle + \beta(T)} + \Gamma'(1) \right) \right) \right] dr_c \right\}^N \quad (24)$$

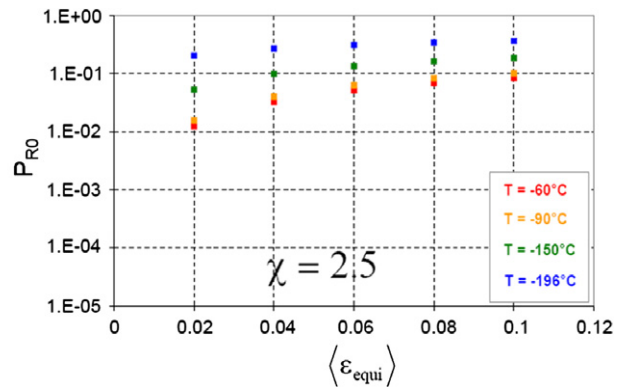
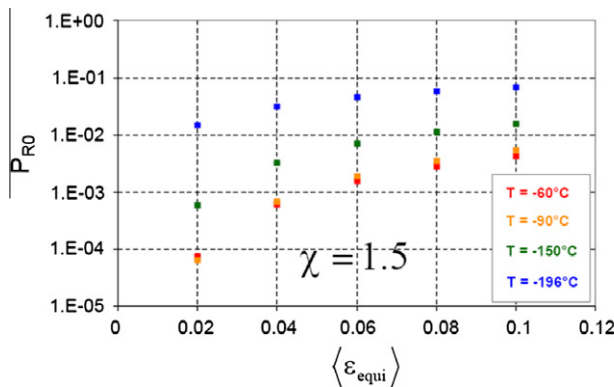


Fig. 18. (a) $\chi = 1.5$, (b) $\chi = 2.5$. Rupture probabilities versus equivalent strain, for different.

with: $\alpha'(T, \chi) = \frac{\sqrt{3}(k-1)}{2k} \alpha(T)$.

$f(r_c)$ is the Lee's distribution obtained by derivation of Eq. (23).

And $N = 125$ is the cells number in the aggregate.

By plotting P_{R0} versus the mean von Mises equivalent plastic strain, we obtain the curves shown in Fig. 18a and b. As a classical result for a given $\langle \varepsilon_{eq} \rangle$, P_{R0} increases with decreasing temperature. Our model also shows a large dependence in terms of loading and temperature.

Fig. 18a and b show that for $\chi = 1.5$ and high temperature, the curves P_{R0} versus $\langle \varepsilon_{eq} \rangle$ are identical. For $\langle \varepsilon_{eq} \rangle = 2\%$, P_{R0} increases of a factor 100 between $T = -60^\circ\text{C}$ and $T = -196^\circ\text{C}$ for $\chi = 2.5$, the increase factor is only equal to 15.

7. Discussion and conclusion

The polycrystal model presented in this paper is the first step of a new approach describing the evolution of plasticity mechanisms with temperature. This approach is devoted to BCC materials presenting a change of the plasticity mechanisms.

An aggregate corresponding to the Elementary Representative Volume is obtained by "columnar" grains, which position and orientation are obtained from an EBSD map ($150 \times 150 \mu\text{m}^2$). The use of a "columnar" 3D aggregate is a shortcut to describe the complex bainitic microstructure. This microstructure is composed of blocks (grains) containing several slightly misoriented (less than 5°) laths. Laths misorientations are neglected here. This means that the initial dislocations mean free path depends on the blocks size. According to observations of Robertson et al. (2007) in A508C13 pressure vessel steel (at low temperature and uni-axial loading), carbides were located on the boundary of the laths, impinging dislocations movement. Lath boundaries appear also to contain dislocation sources. Consequently, dislocations do not easily cross the lath boundaries and the actual mean free path is probably smaller than stated in this study for the small plastic strains. A more accurate simulation should take into account the size effect of the lath. Taking into account the lath and carbide size effect would need a non local approach (Messonnier et al., 2001; Kok et al., 2002; Ma et al., 2006), ignored in our model. Nevertheless, with our simplifying assumptions (limited number of material parameters and simplified microstructure), our results fit with Robertson's measurements (Robertson et al., 2007): the local strain dispersion grows with increasing temperature.

In this paper, the phenomenological equations are derived from discrete dislocations theory and generalized to the continuum dislocations framework. The internal variables are the dislocation densities on the 24 glide systems. At each step of the computation, the densities are then computed in each Gauss point. The mechanical behavior is mainly controlled by the parameters of

the dislocation evolution laws and, in a minor way, by the latent hardening law. Our aim being to describe the material behavior in the plasticity mechanisms transition range, temperature effect is introduced into the constitutive laws. The source and annihilation parameters (named $K(T)$ and $g_c(T)$ respectively), are determined from experimental curves. Note that the $K(T)$ parameter, which is bound to the dislocation mean free path, strongly grows with decreasing temperature, whereas the annihilation parameter $g_c(T)$ is an increasing function of the temperature. At low temperature, such results agree with the weak mobility of the screw dislocations (Robertson et al., 2007) and lead to a weak evolution of the dislocations densities. In fact, parameters of the constitutive laws depend on temperature but also on strain rate and on strain magnitude.

As far as the latent hardening is concerned, the interaction matrix a^{su} is assumed isotropic and independent of temperature and strain amplitude. For high temperature, interaction between dislocations (forest interaction) was extensively studied, and new hardening laws were recently proposed for BCC structure, from Dislocation Dynamics Simulations (Chaussidon et al., 2008; Queyreau et al., 2009). These laws, suitable for the micro-plasticity stage do not describe the mechanical behavior for strain larger than 1%. In this model, the same interaction matrix a^{su} is used for low and high temperature, whatever the plasticity mechanisms and the strain amplitude.

In this paper, the constitutive laws are simple. Many authors (Ma et al., 2006, 2007; Roters et al., 2010) have recently proposed more complex and general hardening laws or a probabilistic approach (Stainier et al., 2002). But, even for the case of single crystals, all these models include a very large number of material parameters and fitting constants that cannot be easily determined.

Experimental validations must be systematically performed and local texture evolution measurements is the most commonly used technique (Raabe and Roters, 2004; Eriau and Rey, 2004). Measurements of some strain components at the surface of the specimen (via micro-grids or spray) were performed (Sachtleber et al., 2002; Sekfali, 2004; St-Pierre et al., 2008). In this paper, the polycrystal aggregate is embedded in the bulk and close to a microcrack tip. Under these conditions, the aggregate is submitted to tri-axial stress field. In such case experimental validation is uneasy. The only available validation is the comparison between the computed texture and a prevision given, for example, by Taylor's model or any other model. For a given stress, at low temperature, average strains are weak (less than 7% in our computation for $T = -90^\circ\text{C}$). However, local strain field may reach up to 30% at -90°C limited to a very small number of elements of the involved meshing. Average local strain being small, no noticeable texture evolution is expected.

To our knowledge, the role of heterogeneous mechanical fields in the rupture process was not previously clarified. Our model is a first attempt to propose an explanation. In our approach, the probability of rupture (which depends on the tri-axial loading and temperature) is partly deduced from the distribution curves of the stress field. Applied by the same authors to compare unirradiated and irradiated materials rupture (Vincent et al., 2010), this model may be considered as a first step towards the study of an actual structure composed of several aggregates.

As a conclusion, this new polycrystal model computes the local strain and stress fields for simplified 3D "columnar" bainitic aggregates. In order to describe the stress pattern ahead of a crack tip, the applied stress corresponds to plane deformation. According to our results, the displacement of the local stress distribution towards larger stress is mainly bound to the increase of the yield stress with decreasing temperature. The maps of deformation and principal stress present different patterns, according to the applied tri-axial loading and to the temperature. Whatever the

temperature, we point out that maxima of the deformation field occur within small bands and that localization increases with high temperature. At low temperature, plasticity stage is very weak. The principal stress field becomes more homogeneous with decreasing temperature. Above -90°C , the maps show maxima of the principal stress within bands crossing grain boundaries or close to some grain boundaries. Below -150°C , the stress bands disappear and stress maxima occur at grain boundaries. Let us note that intergranular or intragranular localization of internal stresses may not be the only source of the rupture. Nevertheless, we have shown that rupture probability is bound to internal stresses distribution within a polycrystal. In the first part of this study, the aggregate is free of carbides, to evaluate the role of the stress heterogeneity. In the second part, a carbide size is introduced to determine the cleavage initiation probability. A comparison with the Beremin criterion (calibrated on experimental data), shows that the scattering of the computed fracture probabilities is of the same order of magnitude than the measured scattering. Temperature and stress tri-axiality ratio have a strong effect on rupture, owing to their influence on plastic strain existing in the volume. We plan to further use the proposed model, to investigate the temperature and constraint effects on fracture toughness.

Acknowledgement

This work was financially supported by European project PER-FECT. A part of mechanical tests was performed at CEA/DEN/SRMA Laboratory, with the kind support of P. Wident and G. Perez.

References

- Astié, P., Peyrade, J.P., Groh, P., 1981. Thermally activated evolution of the dislocation structure generated by low temperature deformation and associated damping phenomena in pure iron. *Journal de Physique. Colloque C5*, supplément au n 10 42, 91–96.
- Barbe, F., Decker, L., Jeulin, D., Cailletaud, G., 2001a. Intergranular and intragranular behavior of polycrystalline aggregates, Part I: F.E. model. *International Journal of Plasticity*, 17, 513–536.
- Barbe, F., Forest, S., Cailletaud, G., 2001b. Intergranular and intragranular behavior of polycrystalline aggregates, Part 2: results. *International Journal of Plasticity*, 17, 537–563.
- Beaudoin, A.J., Dawson, P.R., Mathur, K.K., Kocks, U.F., 1995. A hybrid finite element formulation for polycrystal plasticity with consideration of macrostructural and microstructural linking. *International Journal of Plasticity* 11, 501–521.
- Beremin, F.M., 1983. A local criterion for cleavage fracture of a nuclear pressure vessel steel. *Metallurgical Transactions A* 14, 2277–2287.
- Bhattacharyya, A., El-Danaf, E., Kalidindi, S., Doherty, R., 2001. Evolution of grain scale microstructure during large strain simple compression of polycrystalline aluminum with quasi-columnar grains: OIM measurements and numerical simulations. *International Journal of Plasticity* 17, 861–883.
- Brozzo, P., Buzzicheli, G., Manscanzoni, A., Mirabile, M., 1978. Microstructure and cleavage resistance of low carbon bainitic steels. *Metal Science* 11, 123–129.
- Cailletaud, G., Pilvin, P., 1994. Identification and inverse problems related to material behaviour. In: *Proceedings of the International Seminar on Inverse problems*, Clamart, pp. 79–86.
- Carassou, S., 1999. Idéclenchement du clivage dans un acier faiblement allié: rôle de l'endommagement ductile autour des inclusions. PhD ENSM, Paris.
- Chaussidon, J., Robertson, C., Rodney, D., Fivel, M., 2008. Dislocation dynamics simulation of plasticity in Fe laths at low temperature. *Acta Materialia* 56, 5466–5476.
- Curry, D.A., Knott, J.F., 1978. Effect of microstructure on cleavage fracture stress in mild steel. *Metal Science* 12, 511–514.
- Eriau, P., Rey, C., 2004. Modelling of deformation and rotation bands and of deformation induced grain boundaries in IF steel aggregate during large plane strain compression. *International Journal of Plasticity* 20, 1763–1788.
- Estrin, Y., Mecking, H., 1984. A unified phenomenological description of work hardening and creep based on one-parameter models. *Acta Metallurgica* 32, 57–70.
- Franciosi, P., 1983. Glide mechanisms in B.C.C. crystals: an investigation of the case of iron through multislip and latent hardening tests. *Acta Metallurgica* 31, 1331–1342.
- Hausild, P., Berdin, C., Bompard, P., 2005. Prediction of cleavage fracture for a low-alloy steel in the ductile to brittle transition range. *Material Science and Engineering A* 391, 188–197.

- Hoc, T., Rey, C., Raphanel, J.L., 2001. Experimental and numerical analysis of localization during sequential test for an IF-Ti steel. *Acta Materialia* 49, 1835–1846.
- Keh, A.S., 1964. Work hardening and deformation sub-structure in iron single crystal deformed in tension at 298°K. *Philosophical Magazine* 12, 9–30.
- Kocks, U.F., 1976. Laws for work hardening and low-temperature creep. *Journal of Engineering Materials and Technology*, 76–85.
- Kocks, U.F., Argon, A.S., Ashby, M.F., 1975. *Thermodynamics and kinetics of slip*. Progress in Materials Science. 19. Pergamon Press, Oxford.
- Kok, S., Beaudoin, A.J., Tortorelli, D.A., 2002. A polycrystal plasticity model based on the mechanical threshold. *International Journal of Plasticity* 18, 715–741.
- Kubin, L.P., Louchet, F., Vesely, D., 1978. Description of low-temperature interstitial hardening of the BCC. Lattice from in situ experiments. *Philosophical Magazine A* 38, 205–221.
- Lee, S., Kim, S., Hwang, B., Lee, S., Lee, C.G., 2002. Effect of carbide distribution on the fracture toughness in the transition temperature region of a SA 508 steel. *Acta Materialia* 50, 4755–4762.
- Libert, M., 2007. Etudes expérimentale et numérique de l'effet des mécanismes de plasticité sur la rupture fragile par clivage dans les aciers faiblement alliés. PhD, 2007, Ecole Centrale Paris. Available from: <http://tel.archives-ouvertes.fr>.
- Louchet, F., 1976. Plasticité des métaux de structure cubique centrée à basse température: déformation in-situ par microscopie électronique à haute tension. PhD Université Paul Sabatier Toulouse.
- Ma, A., Roters, F., Raabe, D., 2006. On the consideration of interaction between dislocations and grain boundaries in crystal plasticity finite element modeling. Theory, experiments and simulation. *Acta Materialia* 54, 2181–2194.
- Ma, A., Roters, F., Raabe, D., 2007. A dislocation density based on constitutive law in BCC materials in crystal plasticity FEM. *Computation Material Science* 39, 91–95.
- Mathieu, J.P., 2006. Analyse et modélisation micromécanique du comportement et de la rupture fragile de l'Acier 16MND5: prise en compte des hétérogénéités microstructurales. PhD ENSAM Metz. Available from: <http://pastel.paristech.org>.
- Messonnier, F.T., Busso, E.P., O'Dowd, N.P., 2001. Finite element implementation of a generalised non-local rate-dependent crystallographic formulation for finite strains. *International Journal of Plasticity* 17, 601–640.
- Nemat-Nasser, S., Okinaka, T., Ni, L., 1998. A physically based constitutive model for BCC crystals with application to polycrystalline Tantalum. *Journal of the Mechanics and Physics of Solids* 46, 1009–1038.
- Peirce, D., Asaro, R.J., Needleman, A., 1983. Material rate dependence and localized deformation in crystalline solids. *Acta Metallurgica* 31, 1951–1976.
- Queyreau, S., Monnet, G., Devincere, B., 2009. Slip systems interactions in a-iron determined by dislocation dynamic simulation. *International Journal of Plasticity* 25, 361–377.
- Raabe, D., Roters, F., 2004. Using texture components in crystal plasticity. *International Journal of Plasticity* 20, 339–361.
- Rauch, E., 1993. Etude de l'écrouissage des métaux, aspects microstructuraux et lois de comportement, HDR, Institut National Polytechnique de Grenoble.
- Robertson, C.F., Obertlik, K., Marini, B., 2007. Dislocations structures in 16MND5 pressure vessel steel strained in uniaxial tension at different temperatures from –196 °C up to 25 °C. *Journal of Nuclear Materials* 356, 58–69.
- Roters, F., Eisenlohr, P., Hantcherli, L., Tjahjanto, D.D., Bieler, T.R., Raabe, D., 2010. Overview of constitutive laws, kinematics, homogenization and multiscale methods in crystal plasticity finite element modelling: theory, experiments, applications. *Acta Materialia* 58, 1152–1211.
- Sachtler, M., Zhao, Z., Raabe, D., 2002. Experimental investigation of plastic grain interaction. *Materials Science and Engineering A* 336, 81–87.
- Sekfali, S., 2004. Contribution à l'étude de l'endommagement lié la rupture bimodale des aciers 16MND5. PHD 2004, Ecole Centrale Paris. Available from: <http://tel.archives-ouvertes.fr>.
- Spitzig, W.A., Keh, A.S., 1970a. The effect of orientation and temperature on the plastic flow properties of iron single crystal. *Acta Metallurgica*, 611–622.
- Spitzig, W.A., Keh, A.S., 1970b. The role of internal and effective stresses in the plastic flow of iron single crystals. *Metallurgical Transactions* 1, 3325–3331.
- Stainier, L., Cuitiño, A.M., Ortiz, M., 2002. A micromechanical model of hardening, rate sensibility and thermal softening in bcc single crystals. *Journal of the Mechanics and Physics of Solids* 50, 1511–1545.
- St-Pierre, L., Héripère, E., Dexet, M., Crépin, J., Bertolino, G., Bilger, N., 2008. 3D simulations of microstructure and comparison with experimental microstructure coming from O.I.M analysis. *International Journal of Plasticity* 24, 1516–1532.
- Tabourot, L., Fivel, M., Rauch, E., 1997. Generalised constitutive laws for F.C.C. single crystals. *Materials Science and Engineering A*, 639–642.
- Tang, M., Kubin, L.P., Canova, G.R., 1998. Dislocation mobility and the mechanical response of B.C.C single crystals: a mesoscopic approach. *Acta Materialia* 9, 3221–3235.
- Tanguy, B., Besson, J., Pineau, A., 2003. Comment on effect of carbide distribution on the fracture toughness in the transition temperature region of an AS 508 steel. *Scripta Materialia* 49 (2), 191–197.
- Tanguy, B., Besson, J., Piques, R., Pineau, A., 2005. Ductile to brittle transition of an A508 steel characterized by Charpy impact test, Part II: modelling of the Charpy transition curve. *Engineering Fracture Mechanics* 72, 413–434.
- Teodosiu, C., Raphanel, J.L., Tabourot, L., 1993. Finite element simulation of the large elastoplastic deformation of multicrystals. In: Teodosiu, Raphanel, Sidoroff (Eds.), *MECAMAT'91* © Balkema, Rotterdam, ISBN 90 5410 317 5, pp. 153–160.
- Vincent, L., Libert, M., Marini, B., Rey, C., 2010. Towards a modelling of RPV steel brittle fracture using plasticity computation on polycrystalline aggregates. *Journal of Nuclear Materials* 406 (1), 91–96.
- Yang, W.J., Lee, B.S., Oh, Y.J., Huh, M.Y., Hong, J.H., 2004. Microstructural parameters governing cleavage fracture behaviours in the ductile–brittle transition region in reactor pressure vessel steels. *Materials Science and Engineering A* 379, 17–26.
- Zhang, X.Z., Knott, J.F., 1999. Cleavage fracture in bainitic and martensitic microstructures. *Acta Materialia* 47, 3483–3495.